IEEE Access
Multidisciplinary | Rapid Review | Open Access Journal

Received March 29, 2019, accepted April 8, 2019, date of publication April 22, 2019, date of current version May 23, 2019.

Digital Object Identifier 10.1109/ACCESS.2019.2912305

Near Field Synthesis Based on Multi-Port Antenna Radiation Matrix Eigenfields

RENATO CICCHETTI[1], (Senior Member, IEEE), ANTONIO FARAONE[2], (Senior Member, IEEE), AND ORLANDINO TESTA[1]

[1]Department of Information Engineering, Electronics and Telecommunications, Sapienza University of Rome, 00184 Rome, Italy
[2]Devices Business, Motorola Solutions, Inc., Fort Lauderdale, FL 33322, USA

Corresponding author: Renato Cicchetti (renato.cicchetti@uniroma1.it)

This work was supported by the Italian Ministry of Education, University and Research, under Grant 20152HWRSL.

ABSTRACT The attainable performances of a general formulation employing radiation matrix eigenfields of multi-port antennas to synthesize near-field distributions are investigated. Field synthesis performed on open or closed surfaces, proximate to or enclosing an antenna array, either based on both electric and magnetic target field distributions or just the former, are presented to illustrate the key features of the synthesis technique and its sensitivity with respect to realistic random magnitude and phase variations of the array excitation profiles. Guidelines to perform synthesis and the steering of the complex near-field distributions are then suggested. The propagation characteristics of diffraction-resistant Bessel, OAM Bessel, and Airy beams in their actual finite-energy implementation, when they are excited by finite-size antenna arrays are finally investigated.

INDEX TERMS Airy beams, beam forming, Bessel beams, orbital-angular-momentum (OAM) beams, eigenmodes, eigenfields, multi-port antennas, near-field synthesis, radiation matrix, through-the-wall imaging, wireless power transfer (WPT).

I. INTRODUCTION

The design of modern microwave-sensing devices, high-resolution hyperthermia applicators, through-the-wall imaging equipment, wireless power transfer (WPT) and short-range communication systems, frequently require the synthesis of complex near-field distributions to enhance the resulting performances.

Several approaches have been proposed in literature to realize the aforementioned systems [1]–[7]. Microwave hyperthermia applicators employing antenna arrays to maximize RF energy deposition in patients' tumor tissues were proposed in [1]–[2]. WPT systems based on RF-focusing antenna arrays were developed in [3]–[5], while array systems and suitable detection algorithms for through-the-wall imaging were presented in [6]–[7].

Microwave and quasi-optical diffraction-resistant wave fields were proposed for short-range communications, micromanipulations and RF-focusing [8]–[10]. In [11], optical and millimeter wave high throughput short-range communication systems featuring Bessel beams carrying orbital angular momentum (OAM) to limit beam degradation by obstacles were presented. The optics-based system employs reflective spatial light modulators, while the RF one uses a spiral phase plate to yield an OAM beam from a Gaussian beam, and a metamaterial-based axicon to finally obtain the corresponding order OAM Bessel beam. The spiral plate establishing the required azimuthal phase shift can only be effective at quasi-optical wavelengths.

The generation of high-power Bessel and OAM Bessel beams using lasers was proposed in [12]. This approach yields non-diffractive beams and may be useful for long-range optical links due to their resilience against atmospheric perturbations affecting the field propagation. Finally, in [13], OAM Bessel beams were employed to realize a reflectarray generating cone-shaped radiation patterns in the Ka-band for mobile satellite communications.

In [14], two techniques were proposed to synthesize Airy beams propagating in opposite directions so as to focus electromagnetic energy in the Fresnel region of an array formed by uncoupled, infinitely long thin-wire antennas. The first one employs a linear array, featuring wire current magnitudes and phases given by the sampled Airy wave function over the aperture. The second one requires in-phase feeding of

The associate editor coordinating the review of this manuscript and approving it for publication was Shagufta Henna.

a thin-wire curved array arranged along a $3/2-$power-law surface profile to yield so-called "accelerating beams", showing that oppositely traveling Airy beams yield abruptly-autofocusing beam waves.

The aforementioned solutions, although fulfilling their intended application requirements, all feature static, non-reconfigurable radiative characteristics (e.g., antenna beam and near field angular scan) unless mechanical alterations are dynamically effected. Reconfigurable characteristics (either deterministic or adaptive) would however be desirable, for instance to improve detection accuracy of moving objects, perform selective scans over specific spatial regions inside objects or human subjects, and to sense or communicate beyond propagation obstacles (e.g., pillars and furnishings inside buildings, etc.).

Multiport radiating structures, intrinsically characterized by many degrees of freedom (i.e. radiating elements, their spatial arrangement and excitation profiles) may fulfill the aforementioned requirements if they are suitable to synthesize desirable field distributions in the near or far field region. To this end, this paper addresses the challenge of effecting near field synthesis and steering of complex field distributions (e.g., Bessel and Airy beams) by means of a rather basic square, planar dipole array, employing a novel field synthesis technique recently introduced in literature [15]. This technique exploits newly found, generalized orthogonality properties of the radiation matrix eigenfields, rigorously taking into account couplings among arbitrarily shaped and situated radiating elements, and was shown to provide very good accuracy in spot focusing RF energy and in synthesizing complex near-field distributions on target areas.

In this paper, the aforementioned field synthesis technique is extended to operate on open and closed synthesis surfaces, then used to synthesize target fields expressed in terms of either both $E-$ and $H-$fields or only the $E-$field. Besides comparing their respective synthesis performances, the robustness of the aforementioned techniques is investigated by carrying out a comprehensive sensitivity analysis with respect to random magnitude and phase variations of the array excitation profile, thus quantifying the impact of realistic non-ideal behaviors of the array feeding circuitry. Moreover, the technique is tested on the yet more challenging synthesis of tilted, untilted, and OAM Bessel beams, as well as on Airy beams, characterizing the spatial behavior of such diffraction-resistant field distributions when synthesized by means of a finite-size planar array. Numerical results yield quantitative performance metrics as well as design guidelines for choosing the better performing synthesis approach for the array excitation profile.

The paper is organized in four sections. In Section II, the field synthesis techniques for open and closed surfaces are illustrated. In Section III, the respective performances, including the degradation by random amplitude variations introduced by realistic array feeding circuitry, are compared. In the same Section, synthesis of tilted, untilted, and OAM Bessel beams, as well as Airy beams, are presented and their main propagation characteristics are discussed. Finally, concluding remarks are provided in Section IV.

II. FIELD SYNTHESIS TECHNIQUES

The circuital behavior of multi-port structures (circuits and antennas) can be fully described by the scattering matrix $\underline{\boldsymbol{S}}$, while their energetic behavior can be effectively and advantageously described through a set of Hermitian tensors: radiation matrix $\underline{\boldsymbol{Q}}_{rad}$, loss matrix $\underline{\boldsymbol{Q}}_{loss}$, and reactive power matrix $\underline{\boldsymbol{Q}}_{I}$ as illustrated in [15]. In particular, $\underline{\boldsymbol{Q}}_{rad}$ yields a multi-port antenna active power flow through an arbitrary (open or closed surface) S as

$$P_{rad} = \frac{1}{2}\,\mathrm{Re}\left\{\int_{S\left(\substack{\text{open}\\\text{closed}}\right)} \left[\boldsymbol{E}(\boldsymbol{r}) \times \boldsymbol{H}^{+}(\boldsymbol{r})\right]\cdot\hat{\boldsymbol{n}}\,dS\right\} = \frac{1}{2}\,\boldsymbol{a}^{+}\cdot\underline{\boldsymbol{Q}}_{rad}\cdot\boldsymbol{a} \tag{1}$$

where $\mathrm{Re}\{\cdot\}$ is the real part operator, "+" stands for the Hermitian transpose operator, $\hat{\boldsymbol{n}}$ is the normal unit-vector pointing outward (closed) or away from (open) the surface S, while $\boldsymbol{a}$ is the incident-wave excitation vector at its ports (see Fig. 1). The Poynting theorem states that P_{rad} is the total active power radiated by the multi-port structure when S encloses the antenna ($S = S_{closed}$).

The Hermitian character of the radiation matrix $\underline{\boldsymbol{Q}}_{rad}$ implies the following spectral decomposition

$$\underline{\boldsymbol{Q}}_{rad} = \sum_{i=1}^{N} \lambda_{rad_i}\,\hat{\boldsymbol{v}}_{rad_i}\,\hat{\boldsymbol{v}}_{rad_i}^{+} \tag{2}$$

where λ_{rad_i} and $\hat{\boldsymbol{v}}_{rad_i}$ are the eigenvalues and orthonormal eigenvectors of $\underline{\boldsymbol{Q}}_{rad}$, whose related eigenfields $\boldsymbol{e}_{R_i}(\boldsymbol{r})$ and $\boldsymbol{h}_{R_i}(\boldsymbol{r})$, excited when $\boldsymbol{a} = \hat{\boldsymbol{v}}_{rad_i}$ ($i = 1, 2, ...N$), fulfill the following, noteworthy generalized orthogonality integral relationship [15]

$$\frac{1}{2}\int_{S\left(\substack{\text{open}\\\text{closed}}\right)} \left[\boldsymbol{e}_{R_j}(\boldsymbol{r}) \times \boldsymbol{h}_{R_i}^{+}(\boldsymbol{r}) + \boldsymbol{e}_{R_i}^{+}(\boldsymbol{r}) \times \boldsymbol{h}_{R_j}(\boldsymbol{r})\right]\cdot\hat{\boldsymbol{n}}\,dS = \lambda_{rad_i}\delta_{ij}, \tag{3}$$

δ_{ij} being the Kronecker delta. The eigenvalues λ_{rad_i} express the realized radiation efficiencies (accounting for ohmic, dielectric, coupling, and mismatch losses) of the multiport antenna when $\boldsymbol{a} = \hat{\boldsymbol{v}}_{rad_i}$ and $S = S_{closed}$ encloses the array. The generalized orthogonality condition (3) can be exploited to synthesize target fields on closed or open surfaces as shown in [15], where two field synthesis techniques, denoted as "field-based", were introduced. The first one yields an optimal synthesis when both the target electric and magnetic field distributions are assigned on a given surface, while the second one requires only one of the fields to be assigned,

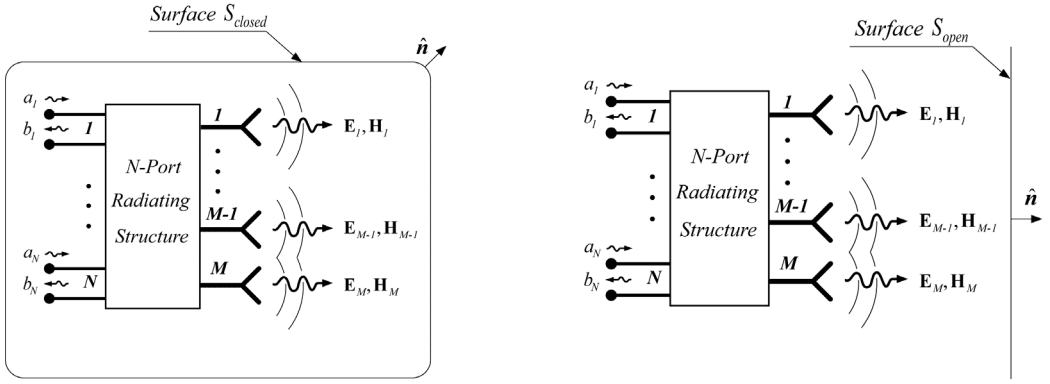

FIGURE 1. Schematic of the N-port radiating structure. The surfaces, (a) closed, and (b) open, on which the field synthesis is performed are shown in the figure.

thus providing a suboptimal synthesis. The optimal array excitation profile is derived as

$$\boldsymbol{a} = \frac{1}{2}\,\underline{\boldsymbol{V}} \cdot \underline{\boldsymbol{\Lambda}}^{-1} \cdot \boldsymbol{V}_{EH}, \tag{4}$$

where $\underline{\boldsymbol{V}} = \left[\hat{\boldsymbol{v}}_{rad_1}, \cdots, \hat{\boldsymbol{v}}_{rad_N}\right]$, $\underline{\boldsymbol{\Lambda}} = diag\left(\lambda_{rad_1}, \cdots, \lambda_{rad_N}\right)$ and $\boldsymbol{V}_{EH}$ is a vector whose components are given by

$$V_{EH_i} = \int\limits_{S\left(\substack{open\\closed}\right)} \left[\boldsymbol{E}(\boldsymbol{r}) \times \boldsymbol{h}_{R_i}^{+}(\boldsymbol{r}) + \boldsymbol{e}_{R_i}^{+}(\boldsymbol{r}) \times \boldsymbol{H}(\boldsymbol{r})\right] \cdot \hat{\boldsymbol{n}}\, dS, \tag{5}$$

$\boldsymbol{E}(\boldsymbol{r})$ and $\boldsymbol{H}(\boldsymbol{r})$ being the aforementioned target fields.

The suboptimal solution, when only the electric field is assigned, is instead given by

$$\boldsymbol{a} = \underline{\boldsymbol{V}} \cdot \left[2\,\underline{\boldsymbol{\Lambda}} - \underline{\boldsymbol{Z}}\right]^{-1} \cdot \boldsymbol{V}_E, \tag{6}$$

with

$$V_{E_i} = \int\limits_{S\left(\substack{open\\closed}\right)} \left[\boldsymbol{E}(\boldsymbol{r}) \times \boldsymbol{h}_{R_i}^{+}(\boldsymbol{r})\right] \cdot \hat{\boldsymbol{n}}\, dS, \tag{7}$$

$$Z_{ij} = \int\limits_{S\left(\substack{open\\closed}\right)} \left[\boldsymbol{e}_{R_i}^{+}(\boldsymbol{r}) \times \boldsymbol{h}_{R_j}(\boldsymbol{r})\right] \cdot \hat{\boldsymbol{n}}\, dS. \tag{8}$$

The optimal synthesis is numerically advantageous as it does not require any matrix inversion since $\underline{\boldsymbol{\Lambda}}$ is diagonal. However, as shown in the next Section in the case of field synthesis on open surfaces, significant numerical accuracy degradation in the field synthesis may occur if eigenfields featuring vanishingly small eigenvalues λ_{rad_i} are employed in Eq. (4), thus it is advisable omitting those eigenfields altogether by introducing a suitable cutoff threshold.

III. NUMERICAL RESULTS

The results presented in this section illustrate features and performances of the proposed techniques in the near-field synthesis on predefined closed or open surfaces, using both target electric and magnetic fields or just the former, as well as in near-field beam synthesis and steering. Target fields consisting of Bessel and Airy beams, characterized by limited diffractive effects [10], [14], and [16]–[18], were chosen due to their applicative relevance, making them suitable for applications in hyperthermia, surface inspections, secure short-range point-to-point communication, particles manipulation, nanosurgery, etc..

The proposed analysis addresses the near-field synthesis accuracy, as well as its sensitivity with respect to the excitation array profile, for a square dipole array using the normalized mean square error ($NMSE$) metric defined in [15] and reported below for the readers' convenience

$$NMSE_{\left(\substack{open\\closed}\right)}\Big|_{dB} = 10\,Log\frac{\displaystyle\int\limits_{S\left(\substack{open\\closed}\right)} \left|\boldsymbol{E}_t^{(Target)} - \boldsymbol{E}_t^{(\mathrm{Synthesized})}\right|^2 dS}{\displaystyle\int\limits_{S\left(\substack{open\\closed}\right)} \left|\boldsymbol{E}_t^{(Target)}\right|^2 dS} \tag{9}$$

to quantify the synthesis accuracy. Irrespective of whether the surface chosen for the field synthesis was open or closed, the parameter $NMSE$ was computed on both an open and a closed surface, so the subscripts "open" and "closed" for $NMSE$ were applied accordingly.

The multi-port array antenna employed in [15], featuring 21×21 $z-$oriented half-wave dipoles (length $145.4\,mm$, radius $1\,mm$) placed a $\lambda_0/4$ away from a $13.6\,\lambda_0 \times 13.6\,\lambda_0$ planar reflector, λ_0 being free-space wavenumber, and excited at $1\,GHz$ by $50\,\Omega$ sources, was adopted in the analysis

TABLE 1. Performance metrics for Bessel beams synthesis on closed surfaces for target areas located at several distances from the array.

E-H-Field Synthesis (*Unfiltered*)					
x_s	$NMSE_{open}$	$\eta_{rad_{open}}$	$NMSE_{closed}$	$\eta_{rad_{closed}}$	P_{in}
λ_0	-22.9 dB	81.9%	-22.6 dB	81.9%	0.965 mW
$2\lambda_0$	-20.0 dB	86.7%	-19.4 dB	86.8%	0.905 mW
$6\lambda_0$	-12.1 dB	83.2%	-11.2 dB	83.9%	0.881 mW
$10\lambda_0$	-8.1 dB	82.0%	-7.3 dB	83.3%	0.791 mW
E-H-Field Synthesis (*Filtered with threshold* $10^{-3}\lambda_{\max}$)					
λ_0	-23.1 dB	86.3 %	-22.8 dB	86.4 %	0.915 mW
$2\lambda_0$	-20.0 dB	87.2 %	-19.4 dB	87.3%	0.899 mW
$6\lambda_0$	-12.1 dB	85.8 %	-11.2 dB	86.5 %	0.855 mW
$10\lambda_0$	-8.1 dB	85.0 %	-7.3 dB	86.4%	0.763 mW

that follows. The dipoles are arranged on a square lattice featuring 180 *mm* (0.6 λ_0) distance between the center-fed dipole ports (5 *mm*−long gap sources). Coupling among dipoles and reflector, as well as diffractive processes, were rigorously modeled by a commercial software based on a full-wave method-of-moments (MoM) (FEKO v. 5.4 by Altair Engineering).

A. FIELD SYNTHESIS ON OPEN AND CLOSED SURFACES

In all cases addressed in the following, the closed surfaces describe a parallelepiped enclosing the antenna with a square base parallel to the array plane, featuring varying heights which identify the field synthesis square surfaces situated at several distances in front of the array.

A preliminary analysis involves the eigenvalues spectra corresponding to open and closed synthesis surfaces (see Fig. 2), where the open surfaces are square faces located in front of the array (see Fig. 1). Energy conservation law requires that the eigenvalues for any closed synthesis surface be independent of its shape. Noteworthy, it was observed that the eigenvalues spectra for open synthesis surfaces situated very close to the array is substantially similar to the closed-surface eigenvalue spectrum, while an increasing number of vanishingly small eigenvalues occur as the distance of the open synthesis surface increases, indicating that a correspondingly growing number of eigenfields spread RF energy outside the open synthesis surface, due in part to the diffractive processes at the array truncation [20]. As anticipated in Section II and remarked in the following, such an analysis of the eigenvalues spectrum is important since, in the synthesis based on target $E-$ and $H-$fields applied on open surfaces, eigenfields featuring vanishingly small eigenvalues could at times produce array excitation profiles causing field synthesis degradation, thus a lower number of eigenfields can be reliably employed for open surface synthesis at increasing distance from the array, de facto reducing the degrees of freedom available in the synthesis itself. Therefore, in the following analysis, synthesis results obtained using all the eigenfields (labeled *unfiltered modal synthesis*) are compared against results derived upon neglecting eigenfields with eigenvalues smaller than $10^{-3}\lambda_{\max}$(labeled *filtered modal synthesis*), $\lambda_{\max}$ being the largest eigenvalue.

A first example involves the synthesis of the zeroth-order finite-support Bessel beam defined in Appendix A, featuring peak amplitude $1V/m$ and radial wavenumber $\beta_\rho = 0.3\,\beta_0$, β_0 being the free-space wavenumber.

In Fig. 3 and 4 the spatial behaviors of the $z-$component of the synthesized electric field at $x_s = \lambda_0$ and $x_s = 10\lambda_0$, both filtered and unfiltered, are reported. The corresponding *NMSE*, efficiency, and incident power figures, including those for the intermediate distances $x_s = 2\lambda_0$ and $x_s = 6\lambda_0$, are provided in Tables 1 and 2 for the synthesis on closed and open target surfaces, respectively. As already mentioned, these performance metrics were computed on both open and closed surfaces, regardless of whether a target surface was closed or open, to derive a complete picture of the synthesis quality, and investigate features, advantages and drawbacks of each approach. For instance, Figs. 3a and 3b show that synthesizing a Bessel beam close to the array roughly yields similar performances for both open and closed synthesis surfaces,

TABLE 2. Performance metrics for Bessel beams synthesis on open surfaces for target areas located at several distances from the array.

E-H-Field Synthesis (*Unfiltered*)					
x_s	$NMSE_{open}$	$\eta_{rad_{open}}$	$NMSE_{closed}$	$\eta_{rad_{closed}}$	P_{in}
λ_0	-19.8 dB	44.5%	-19.4 dB	44.5%	1.777 mW
$2\lambda_0$	-19.0 dB	1.4%	-13.1 dB	1.5%	54.58 mW
$6\lambda_0$	-15.4 dB	0.40%	21.1 dB	49.1%	0.1950 W
$10\lambda_0$	-14.2 dB	0.0000066%	66.7 dB	34.6%	11.658 kW
E-H-Field Synthesis (*Filtered with threshold* $10^{-3}\lambda_{\max}$)					
λ_0	-23.0 dB	86.3 %	-22.4 dB	86.3 %	0.916 mW
$2\lambda_0$	-20.0 dB	86.0%	-18.1 dB	86.5%	0.915 mW
$6\lambda_0$	-14.0 dB	46.1%	0.0 dB	81.2%	1.659 mW
$10\lambda_0$	-9.6 dB	36.1%	2.8 dB	80.6%	1.965 mW

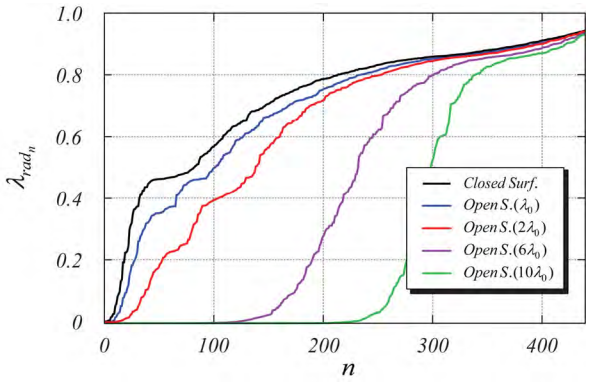

FIGURE 2. Eigenvalues spectrum of the radiation matrix as the distance from the synthesis surface varies. While for short distances from the synthesis surface the eigenvalues spectrum remains substantially similar to that of the closed surface, an increase in the number of vanishingly small eigenvalues can be observed as the distance of the open synthesis surface increases.

as confirmed in Tables 1 and 2 for $x_s = \lambda_0$ and $2\lambda_0$. Such a good agreement between the two techniques is due to the intrinsic limitation of the planar array in directing energy backwards and sideways towards low grazing angles. However, Figs. 3c and 3d show that at larger distances the power flowing through the lateral surfaces may grow significantly (open synthesis surface) unless the field is forced to vanish by a suitable choice of array excitation profiles (closed synthesis surface). This trend is confirmed by the performance data in Tables 1 and 2 ($x_s = 6\lambda_0$ and $10\lambda_0$), upon observing the large dB values attained by the *NMSE* when computed on the closed surface. On the other hand, open surface synthesis may provide better accuracy on the target area, as the smaller *NMSE* figures provided in the tables clearly indicate.

Lateral power flow may be undesirable due to emissions in unwanted directions and the increase in transmit power requirements for the RF electronics feeding the array. This is particularly relevant when the amplitude profiles are derived by synthesis on open surfaces, as shown in Tables 1 and 2 where the array input power P_{in}, defined as the total incident power at the ports, is also reported. For open surface synthesis there can be cases where the target field distribution is well approximated (low $NMSE_{open}$) even though the target-area efficiency is very low, as in the extreme case at $10\lambda_0$ featuring more than 11 kW incident power required, versus only about 0.8 mW needed for closed surface synthesis to obtain comparable error figures. The power flowing to the target area is indeed comparable in the two cases, as it can be readily verified multiplying efficiency and incident power, yet the choice of open surface synthesis has clear disadvantages, including strong undesirable emissions in unwanted directions, from a practical point of view. These drawbacks can be drastically cut down using modal filtering, upon removing from the synthesis process all eigenfields featuring eigenvalues lower than a specific threshold. Adopting an eigenvalue threshold of $10^{-3}\lambda_{\max}$ to limit the energetic impact was found to be effective in reducing lateral power flow for open synthesis surfaces, substantially preserving accuracy in the synthesis plane, as it can be seen comparing Figs. 3 and 4. As expected, modal filtering has a low impact on the lateral energy flow when the field synthesis is performed on closed surfaces. The spatial behavior of the main peak of

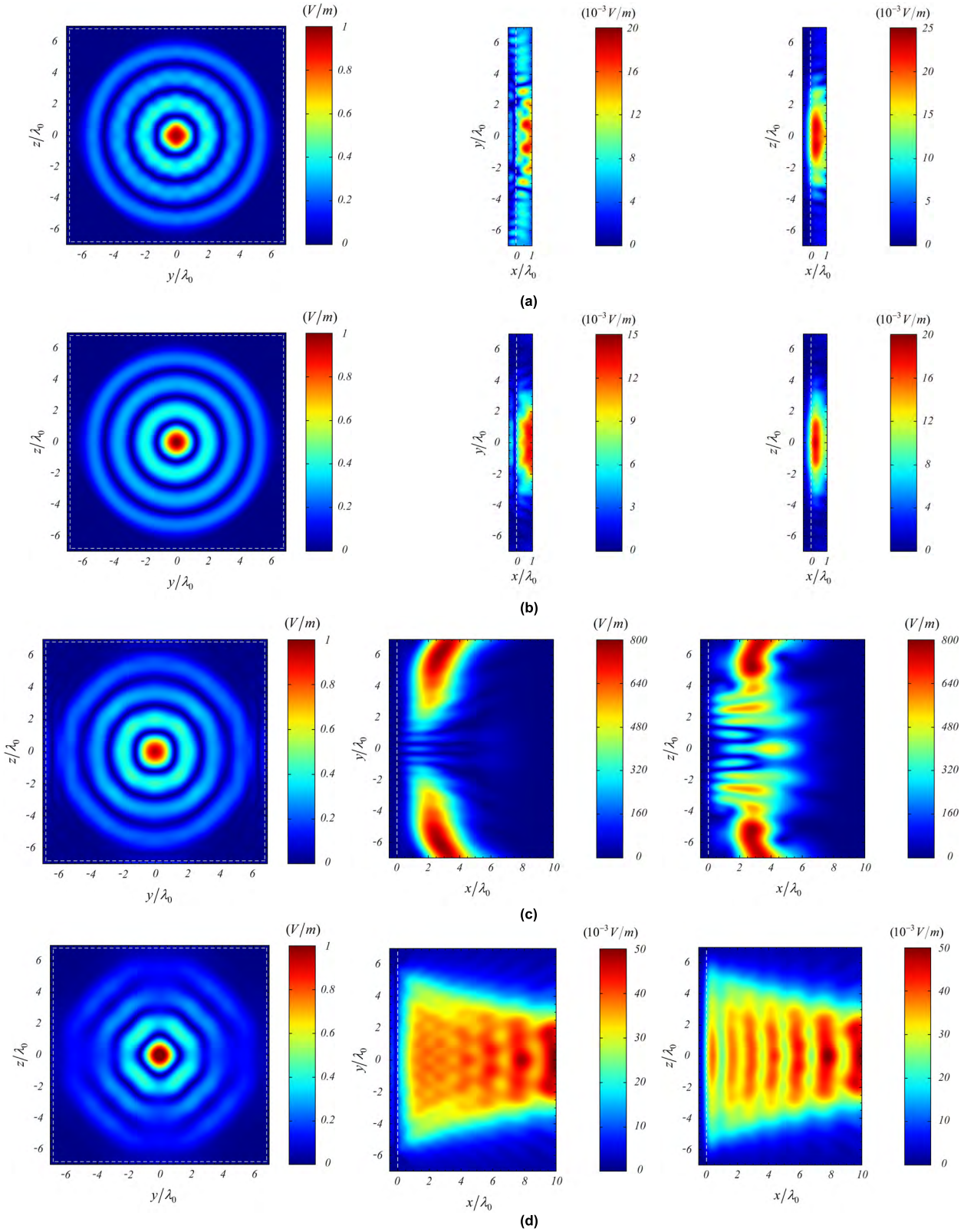

FIGURE 3. Spatial distribution of the electric field (z-component) of a Bessel beam synthesized without any modal filtering on an open surface at (a) $x_S = \lambda_0$, and (c) $x_S = 10\lambda_0$, and on a closed surface at (b) $x_S = \lambda_0$, and (d) $x_S = 10\lambda_0$. The field excited on the lateral surfaces surrounding the array are also shown. A white dashed line outlines the 21 × 21 element array reflector footprint.

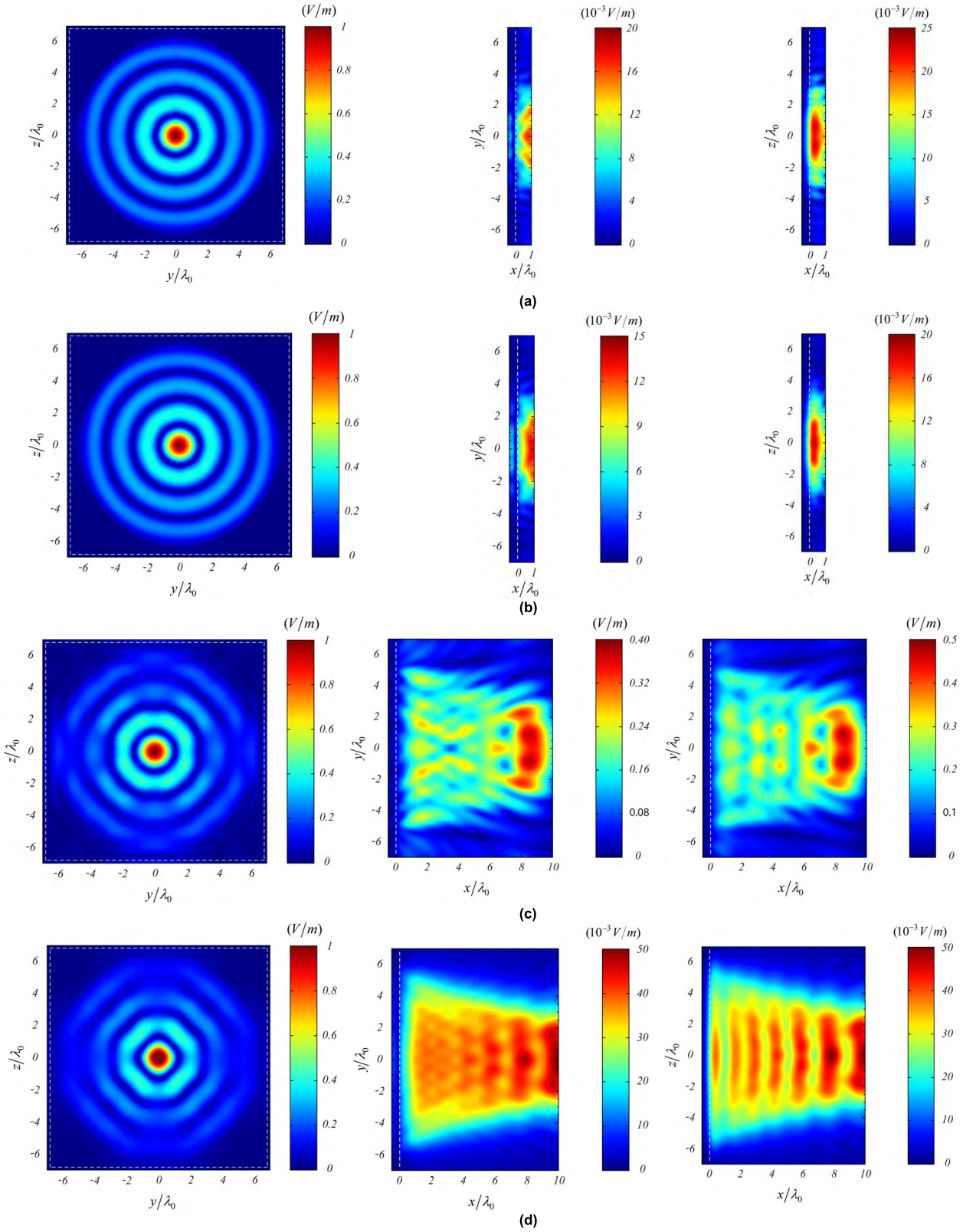

FIGURE 4. Spatial distribution of the electric field (z-component) of a Bessel beam synthesized by applying modal filtering on an open surface at (a) $x_S = \lambda_0$, and (c) $x_S = 10\lambda_0$, and on a closed surface at (b) $x_S = \lambda_0$, and (d) $x_S = 10\lambda_0$. The field excited on the lateral surfaces surrounding the array are also shown. A white dashed line outlines the 21 × 21 element array reflector footprint.

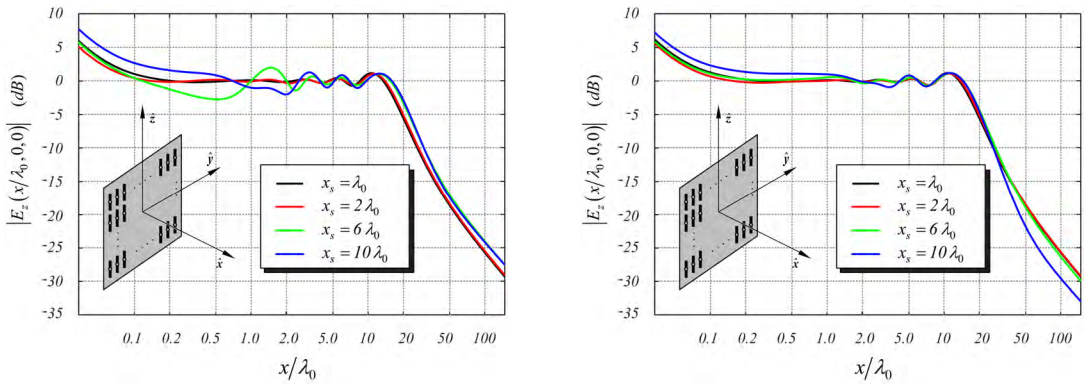

FIGURE 5. Bessel beam electric field magnitude ($z-$component) along the $x-$axis for different x_S synthesis planes. (a) synthesis on open surface, (b) synthesis on closed surface, obtained using modal filtering. Field synthesis on closed surfaces exhibits less ripple than for synthesis on open surfaces, which are characterized by more pronounced yet limited amplitude ripple.

TABLE 3. Performance metrics for Bessel beams synthesis for target areas located at several distances from the array.

E-Field Synthesis (*Unfiltered*) - CLOSED SYNTHESIS SURFACE					
x_s	$NMSE_{open}$	$\eta_{rad_{open}}$	$NMSE_{closed}$	$\eta_{rad_{closed}}$	P_{in}
λ_0	-23.5 dB	86.3%	-22.9 dB	86.3%	0.916mW
$2\lambda_0$	-20.0 dB	87.3%	-19.4 dB	87.4%	0.899 mW
$6\lambda_0$	-12.1 dB	83.6%	-11.3 dB	84.3%	0.878 mW
$10\lambda_0$	-8.0 dB	82.5%	-7.3 dB	83.9%	0.786 mW
E-Field Synthesis (*Filtered with* $10^{-3}\,\lambda_{\max}$) - OPEN SYNTHESIS SURFACE					
λ_0	-23.3 dB	86.4 %	-22.7 dB	86.4 %	0.916 mW
$2\lambda_0$	-20.2 dB	86.8 %	-18.5 dB	87.2%	0.907 mW
$6\lambda_0$	-13.7 dB	42.0 %	0.9 dB	79.9 %	1.825 mW
$10\lambda_0$	-9.4 dB	38.6 %	2.2 dB	81.4%	1.874 mW

the corresponding Bessel beams moving away orthogonally from the array is reported in Fig. 5, for the case of filtered synthesis performed on open and closed surfaces. In both cases the field propagation is essentially tubular up and until the transition towards the spherical wave propagation regime. Smaller ripple is indeed observed in the case of field synthesis performed on closed surfaces.

Tables 1 and 2 also list the realized radiation efficiency $\eta_{rad_{closed}}$, the radiation efficiency $\eta_{rad_{open}}$ relative to the target Bessel beam surface, as well as the incident power P_{in} required collectively at the array ports. All these quantities present quite stable values for closed-surface synthesis, but they may swing widely in the case of open-surface synthesis. From a designer's viewpoint, the closed-surface technique appears to be more attractive due to less demanding dynamical range requisites for the RF circuitry, although its numerical implementation may require evaluating the array field on large domains, especially for distant target areas.

In many practical cases, only the electric (or the magnetic) field distribution needs to be assigned. For instance, this may be the case in applications dealing with electric field synthesis or focusing without any constraint on the corresponding magnetic field (short range communications, heating of lossy materials, etc.). In these instances, the so-called

TABLE 4. NMSE error (closed surface) in presence of a Gaussian dispersion of the excitation profile magnitudes (E-H-field synthesis filtered with threshold $10^{-3}\lambda_{max}$).

	$x_s = 0.5\lambda_0$		$x_s = \lambda_0$		$x_s = 2\lambda_0$		$x_s = 6\lambda_0$		$x_s = 10\lambda_0$	
	MV (dB)	SD (dB)	MV (dB)	SD (dB)	MV (dB)	SD (dB)	MV (dB)	SD (dB)	MV (dB)	SD (dB)
$\sigma_{Mag} = 0\,dB$	-21.8	-	-22.8	-	-19.4	-	-11.2	-	-7.3	-
$\sigma_{Mag} = 0.5\,dB$	-20.0	0.24	-20.7	0.25	-18.3	0.14	-11.1	0.03	-7.2	0.01
$\sigma_{Mag} = 1\,dB$	-16.9	0.47	-17.4	0.49	-16.1	0.36	-10.6	0.09	-7.1	0.05

TABLE 5. NMSE error (closed surface) in presence of a Gaussian dispersion of the excitation profile phases (E-H-field synthesis filtered with threshold $10^{-3}\lambda_{max}$).

	$x_s = 0.5\lambda_0$		$x_s = \lambda_0$		$x_s = 2\lambda_0$		$x_s = 6\lambda_0$		$x_s = 10\lambda_0$	
	MV (dB)	SD (dB)	MV (dB)	SD (dB)	MV (dB)	SD (dB)	MV (dB)	SD (dB)	MV (dB)	SD (dB)
$\sigma_\phi = 0°$	-21.8	-	-22.8	-	-19.4	-	-11.2	-	-7.3	-
$\sigma_\phi = 2°$	-21.1	0.11	-21.9	0.11	-19.0	0.05	-11.2	0.01	-7.3	0.01
$\sigma_\phi = 5°$	-18.5	0.33	-19.0	0.35	-17.3	0.23	-10.9	0.05	-7.2	0.02

$E-$ or $H-$field based synthesis technique [see Eq. (6) for $E-$field synthesis] may be usefully employed [15]. Regarding the $E-$field based approach, comparison of the results reported in Table 3 with those in Tables 1 and 2 indicates that its performances approximate closely those observed using the $E-H$ synthesis technique regardless of the choice of closed or open synthesis surfaces, provided modal filtering is applied to the latter. Designers should be aware of these aspects when choosing a certain approach to near-field synthesis.

Finally, the robustness of the synthesis technique with respect to magnitude and phase variations introduced by the non-ideal behavior of phase shifters, attenuators, and amplifiers [19] used in the RF circuitry realizing the desired array excitation, was estimated. Tables 4 and 5 report computed figures for the *NMSE* mean (*MV*) and standard deviation (*SD*), for the $E-H$ synthesis technique with modal filtering, relative to several different synthesis planes upon assuming random Gaussian probabilistic distributions for magnitude and phase. Fifty Monte Carlo realizations were run for deriving each of several sets of results corresponding to respective magnitude variances $\sigma_{Mag} = 0.5dB$ and $\sigma_{Mag} = 1dB$, and respective phase variances $\sigma_\phi = 2°$ and $\sigma_\phi = 5°$, for the array excitations. The reported analysis generally reveals only a modest quality degradation, induced by the non-ideal behavior of the array feeding network, in the synthesized Bessel beams. Similar trends, which are not reported for the sake of brevity, were observed using the $E-$field based synthesis technique with modal filtering.

B. SYNTHESIS OF TILTED BESSEL BEAMS

Many practical applications may require steerable antenna beams to improve the detection accuracy of moving objects, to scan specific volumes (e.g., around body tumors), or beyond indoor obstacles (e.g., pillars, furnishings) [21]. For instance, one may desire to realize near field wireless links between pair of subarrays located on parallel planes in a multi-point to multi-point communication system (e.g., a wireless, reconfigurable, mobile data bus). In such a case, characterizing the synthesized wave-fields degradation along a chosen propagation path would be of key interest. The excitation profiles yielding the required beams would then be determined upon defining target fields on select synthesis surfaces on a $x = x_s$ plane parallel to the subarray. In Appendix A analytical expressions useful to derive Bessel beam target fields propagating along an arbitrary $\phi-$angle in the xy plane, are provided.

Figs. 6 and 7 show the spatial distribution of the electric field on the synthesis plane placed in $x_s = \lambda_0$ as well as on orthogonal planes to the propagation direction

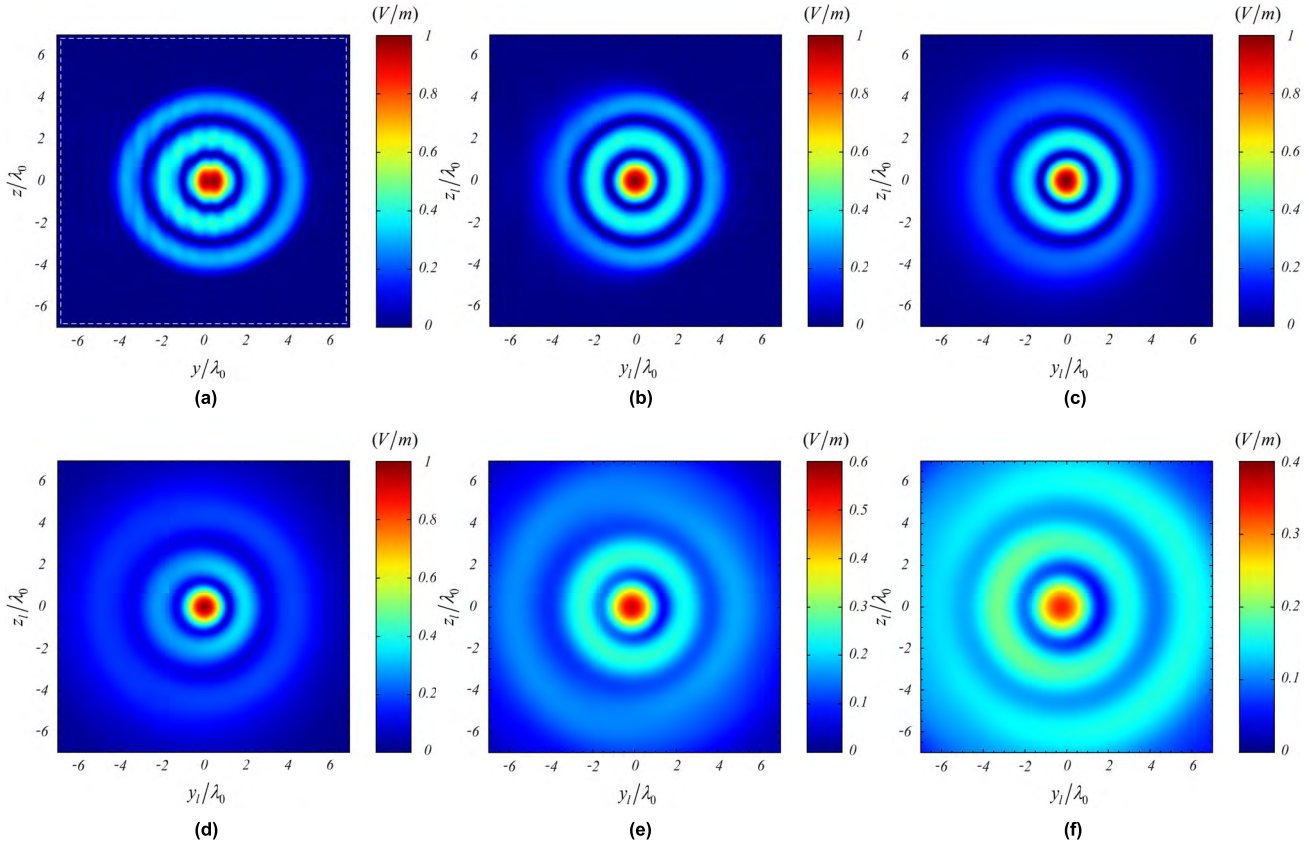

FIGURE 6. Spatial distribution of the electric field (z-component) of the Bessel beam (a) on the synthesis surface at $x_s = \lambda_0$, and along the propagation direction for $\phi = 20°$: (b) $\rho = 2\lambda_0$, (c) $\rho = 5\lambda_0$, (d) $\rho = 10\lambda_0$, (e) $\rho = 15\lambda_0$, and (f) $\rho = 20\lambda_0$. A gradual degradation of the Bessel beam is caused by diffractive processes as the radial observation distance increases.

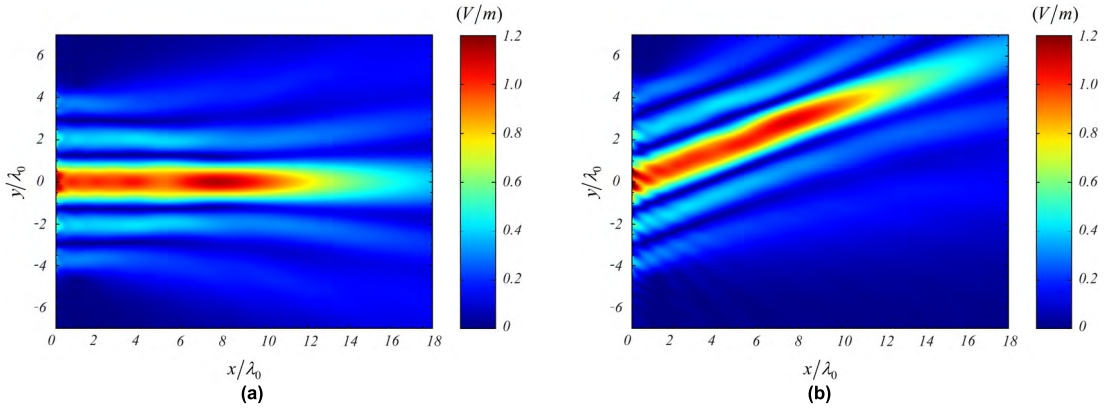

FIGURE 7. Spatial distribution of the electric field (z-component) of the Bessel beam for different tilt angles: (a) $\phi = 0°$, (b) $\phi = 20°$. An interference wave process, which can also be seen in Fig. 6a, is observed near the array when the tilt angle increases.

$\phi = 20°$. Accordingly, a tilted reference frame (y_l, z_l) centered about the $\rho-$axis was employed to plot the spatial distribution of the synthesized field at several distances along the $\rho-$axis. It may be appreciated that the Bessel beam substantially maintains its amplitude and shape up to about $\rho = 10\lambda_0$, then it starts degrading although the main beam is still circumferential even at $\rho = 20\lambda_0$. The main beam amplitude on the $\rho-$axis for different $\phi-$angles up to $\phi = 30°$ is reported in Fig. 8. It is worth observing that the spatial decay, after roughly $10\lambda_0$, features an initial rate that is larger than for spherical decay before settling to the spherical wave propagation regime at about $\rho \simeq 30\lambda_0$. Moreover, the main beam amplitude ripple remains fairly small up to about 10° beam tilt, then increasing

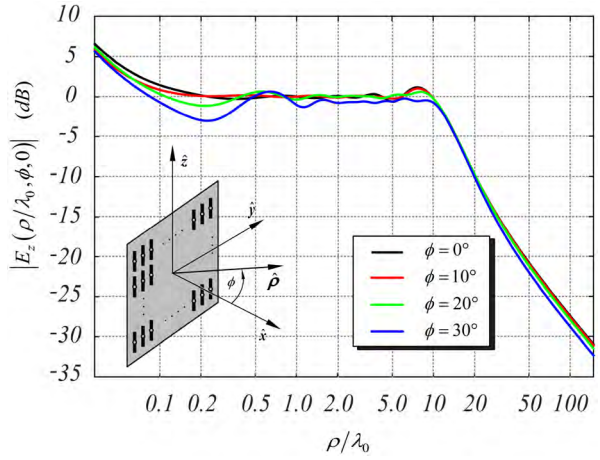

FIGURE 8. Electric field magnitude ($z-$component) for the truncated Bessel beam along the $\rho-$axis for different $\phi-$ angles. Noteworthy is the spatial behavior of the field that, beyond a distance of about $10\lambda_0$, presents a rapid falloff before decaying to the spherical wave propagation regime that occurs at about $30\lambda_0$ from the array surface.

at larger pointing angles. Finally, as observed for broadside beams [10], the starting of the transition towards the spherical propagation regime occurs at a distance which roughly coincides with the vertex of the geometric optics (*GO*) shadow boundary of the Bessel beam field.

C. SYNTHESIS OF OAM BESSEL BEAMS

A second example, consisting of the synthesis of Bessel beams carrying orbital angular momentum (OAM), is presented to show the suitability of the synthesis approach based on the target electric field only in synthesizing accurately such complex magnitude and phase distributions. OAM Bessel beams may be particularly advantageous in real applications due to their interesting "self-healing" properties, which may limit waveform degradation caused by obstacles in free-space optical and RF communication systems [11]–[13] since, under certain conditions, they have been shown to be more robust than non-Bessel OAM beams [11].

The synthesis of OAM beams has been performed using the following target electric field

$$\boldsymbol{E}_t^{(Target)}(\rho,\phi) = J_n\left[\beta_\rho\,\rho\right] circ\left[\frac{\beta_\rho\,\rho}{\xi_{nm}}\right] e^{jn\phi}\hat{\boldsymbol{z}} \qquad (10)$$

where $\beta_\rho = 0.3\,\beta_0$, $circ\,[\cdot]$ is the circle function, while ξ_{nm} is the $m-th$ zero of the $n-th$ order Bessel function.

Magnitude and phase plots for the synthesized OAM Bessel beams at $x_s = \lambda_0$ up to the third order ($m = 3$ for the first two beams, and $m = 2$ for the third one) are reported in Fig. 9. The respective *NMSE* figures ($-25.4dB$, $-23.6dB$, and $-25.7dB$) indicate excellent magnitude and phase

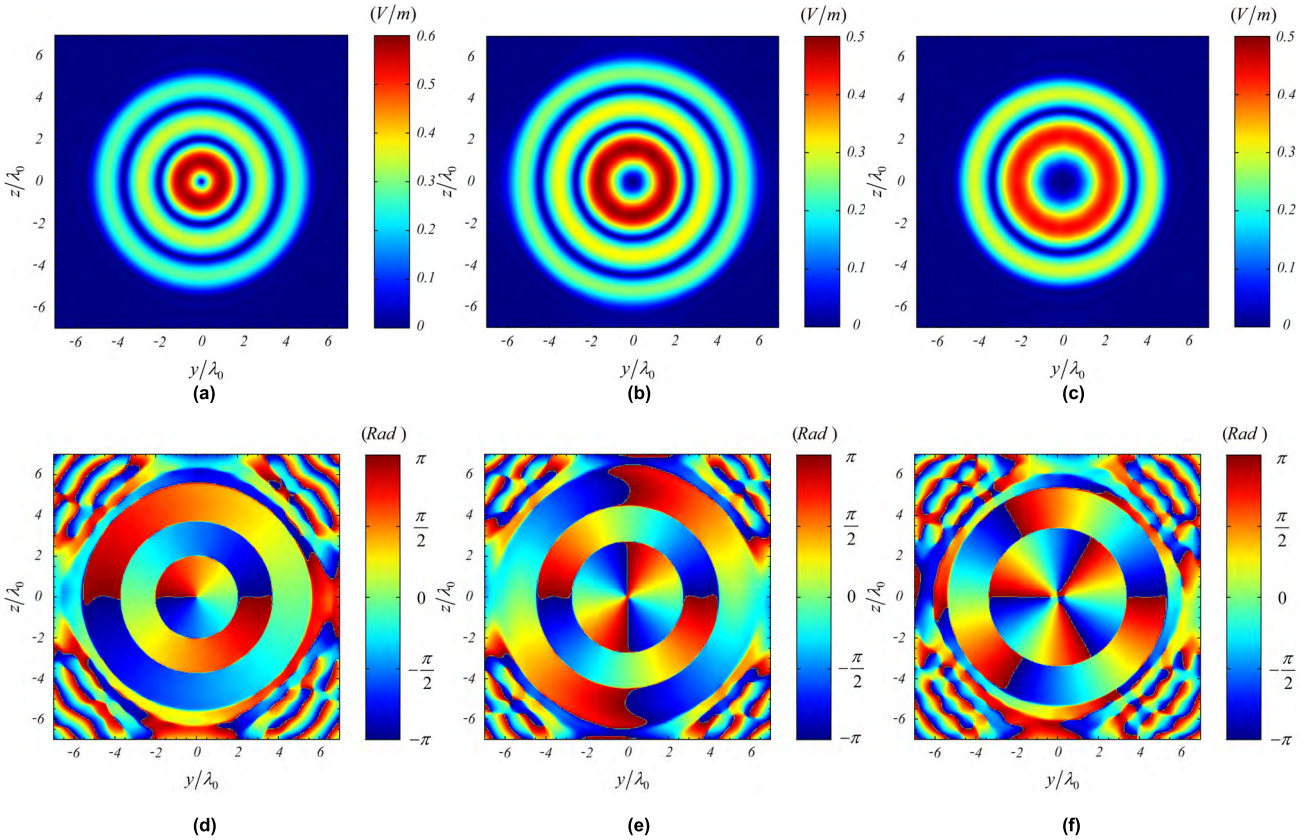

FIGURE 9. Spatial distribution of the magnitude (first-row) and phase (second-row) of the electric field (z-component) of OAM Bessel beams on the synthesis surface at $x_s = \lambda_0$: (a) and (d) first-order, (b) and (e) second-order, and (c) and (f) third-order. An excellent accuracy in the synthesis of the OAM Bessel target field (magnitude and phase) can be observed in the figure.

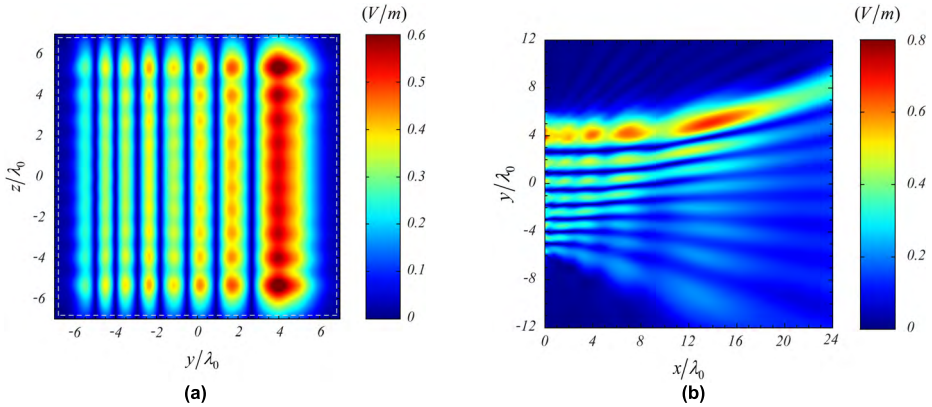

FIGURE 10. Spatial distribution of the electric field (z-component) of the Airy beam computed in the synthesis plane at $x_s = \lambda_0$ (a), and in the xy-plane at z = 0 (b). The peaks appearing in the field map in the yz-plane are related to the maximums of the Airy function even if they suffer from the presence of diffractive processes taking place along the array contour, while the typical parabolic profile of the electric field is observed in the xy-plane. The dashed line outlines the reflector footprint.

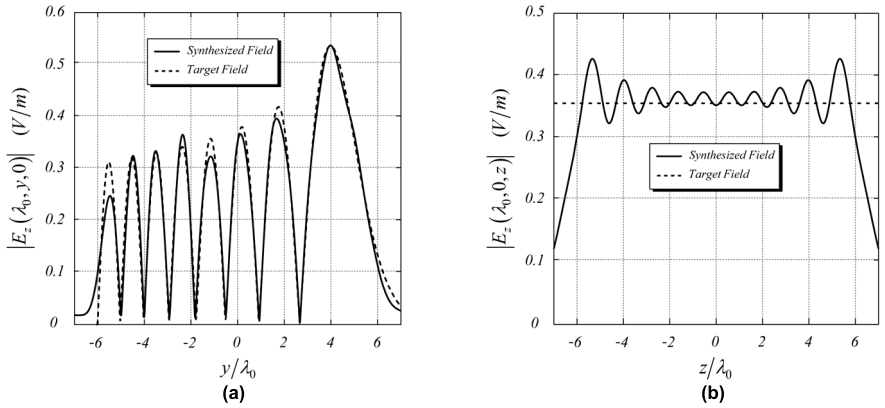

FIGURE 11. Electric field magnitude (z-component) excited at $x_s = \lambda_0$ from the array aperture, for the truncated Airy function with $x_0 = \lambda_0$ computed along the y-direction at z = 0 (a), and along the z-direction at y = 0 (b). A good agreement with the target field can be observed.

accuracy, as required to limit crosstalk between different orbital mode channels [11].

D. SYNTHESIS OF AIRY BEAMS

A further example consists in the synthesis of an Airy beam, a particular field distribution that captured the attention of the optics community due to its diffraction-resistant characteristics enabling a broad range of applications, such as light trajectory control, wavefront self-healing, optical micromanipulation, etc. [14], [16]. A ray-optics analysis of Airy beams reveals that they are characterized by the field propagation occurring on parabolic paths along which most of the RF energy is concentrated [16]. This important feature makes Airy beams useful in micromanipulation of particles [16] or in upcoming applications involving through-the-wall imaging where obstacles may be stationed between the RF source and the electromagnetic target.

The $2-D$ maps of the electric field $z-$component synthesized at $x_s = \lambda_0$ upon assigning the following Airy target field

$$\boldsymbol{E}_t^{(Target)}(y,z) = \begin{cases} Ai\left[\dfrac{y-y_0}{\lambda_0}\right]\hat{z}\ \forall y \in [-6\lambda_0, 7\lambda_0], & z \in [-7\lambda_0, 7\lambda_0] \\ 0, & \text{otherwise} \end{cases} \tag{11}$$

with $y_0 = 5\lambda_0$, are shown in Fig. 10, while the related amplitude profiles along the $y-$direction at $z = 0$, and along the $z-$direction at $y = 0$ are reported in Figs. 11a and 11b, respectively. As shown in Fig. 10, the main beam as well as a few secondary beams follow a parabolic profile along the caustic, while the remaining beams feature an opposite bend in their propagation path due to diffraction at the array truncation. In addition, the diffractive effects occurring along the array contour cause field magnitude fluctuations, clearly visible in Fig. 11. Although the field spatial behavior is in good agreement with the target, a higher error ($NMSE = -11.5dB$) is observed in comparison with the Bessel beam synthesis, due to the larger spatial variations of the Airy target field. This error may be reduced using larger arrays.

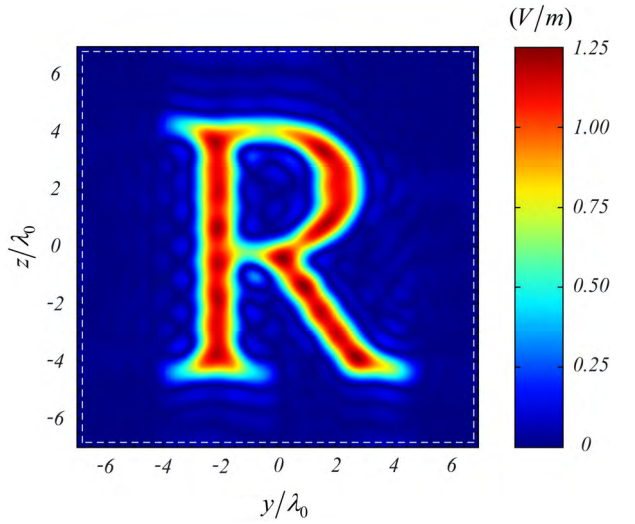

FIGURE 12. Spatial distribution of the electric field (z-component) of the R-shaped beam synthesized on closed surface at $x_s = \lambda_0$. An excellent agreement with the target field is observed. The white dashed line outlines the 21 × 21 element array reflector footprint.

E. SYNTHESIS OF STRONGLY ASYMMETRIC FIELDS

The last example features the synthesis of a strongly asymmetric near field beam, consisting of the Times New Roman character "R". In Fig. 12 the $2-D$ map, computed at $x_s = \lambda_0$, of the $z-$polarized electric field having unit amplitude in the domain corresponding to the character "R" is reported to show the flexibility of the $E-$field synthesis approach applied to arbitrary target fields. As it can be observed also in this case the agreement with the target field is excellent ($NMSE = -8.6dB$).

IV. CONCLUSIONS

A field synthesis procedure, based on the eigenfields of the radiation matrix of a multiport radiating structure, was employed to synthesize near fields having complex spatial distributions. The numerical results showed that near-field synthesis performed by means of target electric and magnetic fields exhibits numerical accuracy similar to those based on the target electric field alone. In addition, it has been observed that field synthesis performed on open surfaces feature a higher accuracy within the target area but much smaller accuracy outside, whereas synthesis based on closed target field surfaces are more burdensome numerically but extremely more accurate outside the target area, particularly at large distance from the array surface. Nevertheless, the two approaches provide similar numerical accuracy when the synthesis surfaces are close to the array, or when modal filtering is suitably applied to remove eigenfields featuring low efficiency. In fact, while for the synthesis on closed surfaces the modal filtering has a very limited impact, it assumes a key role to synthesize good quality field distributions on open surfaces located far from the array plane. This finding may be exploited for reducing the computational burden especially in real-time tracking applications. Finally, propagation characteristics of diffraction-resistant Bessel, OAM Bessel and Airy beams in their actual finite-energy implementation, when excited by antenna arrays of finite dimensions, have been investigated. Bessel beams were found to decay towards the spherical wave propagation regime at about the same distance for different beam tilt angles, while synthesized Airy beams propagate along parabolic caustics except for far secondary beams placed near the array boundary due to diffractive effects occurring at the array truncation. Based on the foregoing analysis, the proposed near-field technique appears to be suitable for deriving array excitation profiles that may synthesize accurately uncommonly complex near field distributions.

APPENDIX

The target fields employed to synthesize Bessel beams are given by

$$E_y(x,y,z) = 0 \tag{A1}$$

$$E_z(x,y,z) = E_0 J_0\left(\beta_\rho \sqrt{y^2+z^2}\right) circ\left[\frac{\beta_\rho \sqrt{y^2+z^2}}{\xi_{04}}\right] e^{-jx\sqrt{\beta_0^2-\beta_\rho^2}} \tag{A2}$$

$$H_y(x,y,z) = -\frac{E_0}{\eta_0}\frac{\beta_\rho^2}{\gamma\,\beta_0}\left[\left(\frac{\beta_0^2}{\beta_\rho^2}-\frac{y^2}{y^2+z^2}\right) J_0\left(\beta_\rho\sqrt{y^2+z^2}\right) + \frac{1}{\beta_\rho\sqrt{y^2+z^2}}\,\frac{y^2-z^2}{y^2+z^2}\,J_1\left(\beta_\rho\sqrt{y^2+z^2}\right)\right]\cdot circ\left[\frac{\beta_\rho\sqrt{y^2+z^2}}{\xi_{04}}\right] e^{-jx\sqrt{\beta_0^2-\beta_\rho^2}} \tag{A3}$$

$$H_z(x,y,z) = \frac{E_0}{\eta_0}\frac{\beta_\rho^2}{\gamma\,\beta_0}\,\frac{yz}{y^2+z^2}\left[J_0\left(\beta_\rho\sqrt{y^2+z^2}\right) - \frac{2}{\beta_\rho\sqrt{y^2+z^2}}\,J_1\left(\beta_\rho\sqrt{y^2+z^2}\right)\right]\cdot circ\left[\frac{\beta_\rho\sqrt{y^2+z^2}}{\xi_{04}}\right] e^{-jx\sqrt{\beta_0^2-\beta_\rho^2}} \tag{A4}$$

with

$$\gamma = \sqrt{\beta_0^2-\beta_\rho^2}, \tag{A5}$$

where E_0 defines the maximum value of the electric field amplitude, $circ\,[\cdot]$ is the circle function and $\xi_{04} \simeq 11.7915$ is the fourth zero of the zeroth order Bessel function, η_0 is the free-space characteristic impedance, while β_0 and β_ρ are the free-space and the radial wavenumbers, respectively. The target field components useful for the synthesis of tilted Bessel beams, rotated by an angle ϕ in the xy plane, can be evaluated using the usual transformation formulas between orthogonal coordinate systems.

ACKNOWLEDGMENT

The authors are grateful to Dr. G. (Goga) Bit-Babik at the Motorola Solutions Chief Technology Office for his expert

assistance in MoM simulation analysis and M. Mazzetta of the University of Rome "La Sapienza" for IT technical support.

REFERENCES

[1] F. Tofigh, J. Nourinia, M. Azarmanesh, and K. M. Khazaei, "Near-field focused array microstrip planar antenna for medical applications," *IEEE Antennas Wireless Propag. Lett.*, vol. 13, pp. 915–954, 2014.

[2] X. He, W. Geyi, and S. Wang, "Optimal design of focused arrays for microwave-induced hyperthermia," *IET Microw., Antennas Propag.*, vol. 9, no. 14, pp. 1605–1611, Nov. 2015.

[3] N. Shinohara, "Power without wires," *IEEE Microw. Mag.*, vol. 12, no. 7, pp. S64–S73, Dec. 2011.

[4] G. Oliveri, L. Poli, and A. Massa, "Maximum efficiency beam synthesis of radiating planar arrays for wireless power transmission," *IEEE Trans. Antennas Propag.*, vol. 61, no. 5, pp. 2490–2499, May 2013.

[5] H. Sun and W. Geyi, "Optimum design of wireless power transmission systems in unknown electromagnetic environments," *IEEE Access*, vol. 5, pp. 20198–20206, Oct. 2017.

[6] K. E. Browne, R. J. Burkholder, and J. L. Volakis, "Through-wall opportunistic sensing system utilizing a low-cost flat-panel array," *IEEE Trans. Antennas Propag.*, vol. 59, no. 3, pp. 859–868, Mar. 2011.

[7] G. Gennarelli, G. Vivone, P. Braca, F. Soldovieri, and M. G. Amin, "Multiple extended target tracking for through-wall radars," *IEEE Trans. Geosci. Remote Sens.*, vol. 53, no. 12, pp. 6482–6494, Dec. 2015.

[8] P. Lemaitre-Auger, S. Abielmona, and C. Caloz, "Generation of Bessel beams by two-dimensional antenna arrays using sub-sampled distributions," *IEEE Trans. Antennas Propag.*, vol. 61, no. 4, pp. 1838–1849, Apr. 2013.

[9] D. McGloin, V. Garcés-Chávez, and K. Dholakia, "Interfering Bessel beams for optical micromanipulation," *Opt. Lett.*, vol. 28, no. 8, pp. 657–659, Apr. 2003.

[10] D. McGloin and K. Dholakia, "Bessel beams: Diffraction in a new light," *Contemp. Phys.*, vol. 46, no. 1, pp. 15–28, Jan./Feb. 2005.

[11] N. Ahmed *et al.*, "Mode-division-multiplexing of multiple Bessel-Gaussian beams carrying orbital-angular-momentum for obstruction-tolerant free-space optical and millimetre-wave communication links," *Sci. Rep.*, vol. 6, Mar. 2016, Art. no. 22082.

[12] X. Chu, Q. Sun, J. Wang, P. Lü, W. Xie, and X. Xu, "Generating a Bessel-Gaussian beam for the application in optical engineering," *Sci. Rep.*, vol. 5, Dec. 2015, Art. no. 18665.

[13] M. Veysi, C. Guclu, F. Capolino, and Y. Rahmat-Samii, "Revisiting orbital angular momentum beams: Fundamentals, reflectarray generation, and novel antenna applications," *IEEE Antennas Propag. Mag.*, vol. 60, no. 2, pp. 68–81, Apr. 2018.

[14] I. D. Chremmos, G. Fikioris, and N. K. Efremidis, "Accelerating and abruptly-autofocusing beam waves in the fresnel zone of antenna arrays," *IEEE Trans. Antennas Propag.*, vol. 61, no. 10, pp. 5048–5056, Oct. 2013.

[15] R. Cicchetti, A. Faraone, and O. Testa, "Energy-based representation of multiport circuits and antennas suitable for near- and far-field syntheses," *IEEE Trans. Antennas Propag.*, vol. 67, no. 1, pp. 85–98, Jan. 2019.

[16] J. Baumgartl, M. Mazilu, and K. Dholakia, "Optically mediated particle clearing using Airy wavepackets," *Nature Photon.*, vol. 2, pp. 675–678, Nov. 2008.

[17] W. Wen and X. Chu, "Quantitative comparison of self-healing ability between Bessel–Gaussian beam and Airy beam," *Ann. Phys.*, vol. 360, pp. 549–555, Sep. 2015.

[18] R. Kadlimatti and P. V. Parimi, "Millimeter-wave nondiffracting circular Airy OAM beams," *IEEE Trans. Antennas Propag.*, vol. 67, no. 1, pp. 260–269, Jan. 2019.

[19] K. Liu *et al.*, "Generation of OAM beams using phased array in the microwave band," *IEEE Trans. Antennas Propag.*, vol. 64, no. 9, pp. 3850–3857, Sep. 2016.

[20] Ö. A. Çivi, P. H. Pathak, H.-T. Chou, and P. Nepa, "A hybrid uniform geometrical theory of diffraction–moment method for efficient analysis of electromagnetic radiation/scattering from large finite planar arrays," *Radio Sci.*, vol. 35, no. 2, pp. 607–620, Mar./Apr. 2000.

[21] P. Bernardi, R. Cicchetti, and O. Testa, "An accurate UTD model for the analysis of complex indoor radio environments in microwave WLAN systems," *IEEE Trans. Antennas Propag.*, vol. 52, no. 6, pp. 1509–1520, Jun. 2004.

RENATO CICCHETTI (S'83–M'83–SM'01) was born in Rieti, Italy, in 1957. He received the Laurea degree *(summa cum laude)* in electronics engineering from the Sapienza University of Rome, Rome, Italy, in 1983. From 1983 to 1986, he was an Antenna Designer with Selenia Spazio S.p.A. (now Thales Alenia Space S.p.A.), Rome, where he was involved in the studies on theoretical and practical aspects of antennas for space application and scattering problems. From 1986 to 1994, he was a Researcher, and from 1994 to 1998, he was an Assistant Professor with the Department of Electronics Engineering, Sapienza University of Rome, where he is currently a Full Professor. He was a Visiting Professor with the Motorola Florida Corporate Electromagnetics Research Laboratory, Fort Lauderdale, FL, USA, in 1998, 2002, and 2006, where he was involved in antennas for cellular and wireless communications. Since 2012, he has been the Lead Editor of the annual special issue on Wideband, Multiband, Tunable, and Smart Antenna Systems For Mobile UWB Wireless Applications for the *International Journal of Antennas and Propagation*, while he is currently one of the coordinators of the research project ultra-wideband virtual imaging extra wall for high-penetration, high-quality imagery of enclosed structures (U-VIEW) supported by the Italian Ministry of Education, University and Research (MIUR). His current research interests include electromagnetic field theory, asymptotic techniques, electromagnetic compatibility, wireless communications, microwave and millimeter-wave integrated circuits, and antennas. He is a Member of the Italian Electromagnetic Society (*SIEm*), and his results listed in Marquis *Who's Who in the World* and *Who's Who in Science and Engineering*.

ANTONIO FARAONE (M'97–SM'05) was born in Rome, Italy, in 1966. He received the Ph.D. degree in applied electromagnetics from the Sapienza University of Rome Sapienza, in 1997, then he joined the Motorola (now Motorola Solutions, Inc.) Corporate Electromagnetic Energy (EME) Research Laboratory, Fort Lauderdale, FL, USA, where he is currently involved in mobile antenna technology and RF dosimetry research, and RF exposure safety and product compliance standards development. He currently oversees RF exposure compliance matters as the Chief EME Scientist with Motorola Solutions, where he is a Scientific Advisory Board Associates (SABA) Member, Master Innovator, and Dan Noble Fellow. He holds 37 patents, mostly in antenna technologies. He has coauthored 36 refereed journal publications, and he continues to be actively involved in the IEEE and IEC standards related to safe EME exposure. He currently serves as the Chair of the Mobile & Wireless Forum, an international industry association supporting research into RF health and safety and promoting device integrity and accessibility.

ORLANDINO TESTA was born Minturno, Italy, in 1972. He received the Laurea degree *(cum laude)* in electronic engineering and the Ph.D. degree from the Sapienza University of Rome, Rome, Italy, in 1997 and 2003, respectively. Since 2001, he has been the High School Teacher with I.T.I.S. G. Armellini, Institute of Rome, where he is involved in teaching electronics and telecommunications. He is also currently collaborating with the Department of Electronic Engineering, Sapienza University of Rome. He is currently studying high-frequency models for the analysis of radio coverage in indoor environments and tunnels with a particular attention to EMC/EMI problems. His main research interests include propagation and the radiation of electromagnetic fields, electromagnetic compatibility, microwave and millimeter-wave integrated circuits, and antennas.